J. Fluid Mech. (2007), *vol.* 582, *pp.* 449–461.
doi:10.1017/S0022112007006349 Printed in the United Kingdom

Passive scalar mixing in vortex rings

RAJES SAU AND KRISHNAN MAHESH

Aerospace Engineering & Mechanics, University of Minnesota, Minneapolis, MN 55455, USA

(Received 17 November 2006 and in revised form 27 February 2007)

Direct numerical simulation is used to study the mixing of a passive scalar by a vortex ring issuing from a nozzle into stationary fluid. The 'formation number' (Gharib *et al. J. Fluid Mech.* vol. 360, 1998, p. 121), is found to be 3.6. Simulations are performed for a range of stroke ratios (ratio of stroke length to nozzle exit diameter) encompassing the formation number, and the effect of stroke ratio on entrainment and mixing is examined. When the stroke ratio is greater than the formation number, the resulting vortex ring with trailing column of fluid is shown to be less effective at mixing and entrainment. As the ring forms, ambient fluid is entrained radially into the ring from the region outside the nozzle exit. This entrainment stops once the ring forms, and is absent in the trailing column. The rate of change of scalar-containing fluid is found to depend linearly on stroke ratio until the formation number is reached, and falls below the linear curve for stroke ratios greater than the formation number. This behaviour is explained by considering the entrainment to be a combination of that due to the leading vortex ring and that due to the trailing column. For stroke ratios less than the formation number, the trailing column is absent, and the size of the vortex ring increases with stroke ratio, resulting in increased mixing. For stroke ratios above the formation number, the leading vortex ring remains the same, and the length of the trailing column increases with stroke ratio. The overall entrainment decreases as a result.

1. Introduction

The motion of a fluid column of length L through an orifice of diameter D produces a vortex ring. Vortex rings have been studied by many researchers, and a large volume of work exists (see e.g. the review by Shariff & Leonard 1992). This paper is motivated by experimental observations on the use of pulsing to control the mixing characteristics of free jets (e.g. Vermeulen, Ramesh & Yu 1986; Vermeulen, Rainville & Ramesh 1992), and jets in crossflow (e.g. Johari, Pacheco-Tougas & Hermanson 1999; Eroglu & Briedenthal 2001; M'Closkey *et al.* 2002). Pulsing of the jet is seen to result in the formation of vortex rings, whose strength and spacing are dictated by the frequency and duty cycle of the jet. The resulting flow appears to improve the mixing rate and increase the entrainment. This paper examines the basic problem of how a vortex ring mixes with stationary fluid.

Most past work has studied vortex ring formation and kinematics (e.g. Maxworthy 1977; Didden 1979). The temporal evolution of vortex circulation during ring formation (Didden 1979; Glezer 1988), and during the post-formation phase (Maxworthy 1972) have been discussed. The total circulation and impulse have been shown to be approximately equal, for nozzles with and without a wall at the exit plane (James & Madnia 1996). Gharib, Rambod & Shariff (1998) show that for a stroke ratio, defined as the ratio of the stroke length to the nozzle exit diameter, of

around 4, the flow transitions from a coherent vortex ring to a ring with a trailing jet. They refer to this critical stroke ratio as the 'formation number'. The vortex ring is shown to achieve its maximum circulation at the formation number. Universality of the formation number was confirmed by generating vortex rings with different nozzle exit diameters, boundaries and non-impulsive piston velocities. Rosenfeld, Rambod & Gharib (1998) numerically studied the effect of the time history of the velocity, velocity profile, vortex generator geometry and Reynolds number on the formation number. They found that the formation number appears independent of Reynolds number.

The entrainment characteristics of vortex rings were studied by Müller & Didden (1980) who estimated the entrainment fraction to be approximately 40 % using a dye marker in their experiment. Dabiri & Gharib (2004) experimentally examined entrainment; their computed entrainment fraction was found to lie within 30 % to 40 % for stroke ratios of 2 and 4. They used counterflow protocols to improve the entrainment fraction to 65 %. Their experiments do not resolve the convective fluid entrainment that occurs during the vortex ring formation. A computational study by James & Madnia (1996) examined entrainment and scalar mixing by vortex rings. However, their simulations were limited to small stroke ratios ($L/D < 4$), and do not cover the effect of stroke ratio.

The objective of the present investigation is to study passive scalar mixing and entrainment by vortex rings in stationary fluid, for a range of stroke ratios encompassing the formation number. The entrainment of ambient fluid during ring formation is studied. Mixing and entrainment in the two regimes defined by formation number are contrasted. The flow field in these two regimes is characterized by two different structures – a single vortex ring and a vortex ring with trailing column. We seek the structure which is more efficient in mixing with ambient fluid. The effect of Schmidt number on this behaviour is also considered.

The paper is organized as follows. The problem is defined and simulation details are described in § 2. Simulation results for the vorticity field, circulation, and entrainment fraction are compared to experimental results in § 3.1. In § 3.2, passive scalar mixing in vortex rings is examined in detail. Entrainment during ring formation is discussed in § 3.2.2. The effect of stroke ratio on the rate of volume mixing is studied in § 3.2.3. The paper ends with a brief summary in § 4.

2. Simulation details

2.1. *Problem statement*

Figure 1(*a*) shows a schematic of the problem, where a slug of fluid is pushed through a cylindrical nozzle of 3:1 diameter ratio. The origin is located at the centre of the nozzle exit plane, and the nozzle axis points in the y-direction. The piston is modelled by specifying a time-dependent velocity field (square wave pulse) at the nozzle inlet (e.g. Rosenfeld *et al.* 1998). A top-hat velocity profile (U_{in}) is specified at the nozzle inflow for a duration of time τ (referred to as the piston time duration). The inflow velocity is zero for time greater than τ. The stroke length and non-dimensional time are determined using the mean nozzle exit velocity, $\overline{U}_{exit}$ which denotes the equivalent piston velocity. The stroke length $L = \overline{U}_{exit}\tau$. The stroke ratio ($L/D$), defined as the ratio of the stroke length (L) to the nozzle exit diameter (D) is equal to $\overline{U}_{exit}\tau/D$. The stroke ratio is varied by changing the piston time duration τ. The Reynolds number of the flow based on $\overline{U}_{exit}$ and nozzle exit diameter (D) is 600. The non-dimensional time, $t^* = \overline{U}_{exit}t/D$, is referred to as the formation time (Gharib *et al.* 1998). The simulations are performed for stroke ratios varying from 1.6 to 8.

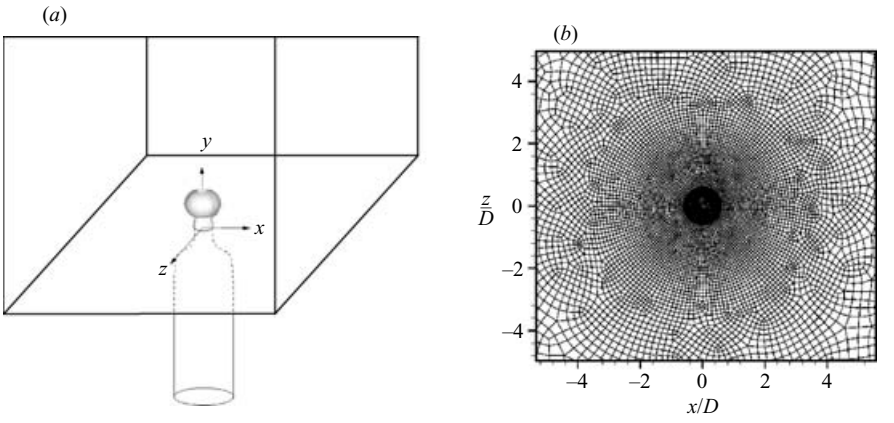

FIGURE 1. (*a*) A schematic of the problem. Note the vortex ring generated by the fluid emerging out of the nozzle exit. (*b*) A horizontal slice of the mesh.

2.2. *Numerical details*

The numerical scheme solves the incompressible Navier–Stokes equations

$$\frac{\partial u_i}{\partial t} + \frac{\partial u_i u_j}{\partial x_j} = -\frac{\partial p}{\partial x_i} + \nu \frac{\partial^2 u_i}{\partial x_j x_j}, \quad \frac{\partial u_i}{\partial x_i} = 0. \tag{2.1}$$

on unstructured grids. Here u_i, p and ν denote the velocities, pressure and kinematic viscosity respectively. The density of the fluid is assumed constant and is absorbed into the pressure. The numerical scheme has been described in detail by Mahesh, Constantinescu & Moin (2004). The algorithm stores the Cartesian velocities and the pressure at the centroids of the cells (control volumes) and the face normal velocities are stored independently at the centroids of the faces. The scheme is a predictor–corrector formulation which emphasizes discrete energy conservation on unstructured grids. This property makes the algorithm robust at high Reynolds numbers without numerical dissipation. The predicted velocities at the control-volume centroids are obtained using the viscous and the nonlinear terms of equation (2.1) which are then used to predict the face normal velocities on the faces. The predicted face normal velocity is projected so that continuity is discretely satisfied. This yields a Poisson equation for pressure which is solved iteratively using a multigrid approach. The pressure field is used to update the Cartesian control-volume velocities. Implicit time-stepping is performed using a Crank–Nicholson scheme. The algorithm has been validated for a variety of problems over a range of Reynolds numbers (Mahesh *et al.* 2004).

The passive scalar is computed by solving the advection–diffusion equation

$$\frac{\partial C}{\partial t} + \frac{\partial C u_j}{\partial x_j} = \frac{\nu}{Sc} \frac{\partial^2 C}{\partial x_j x_j}, \tag{2.2}$$

where C is the concentration of the scalar. The fluid emerging from the nozzle exit has a value of $C = 1.0$, and the ambient fluid has $C = 0$. The spatial derivatives are computed using a predictor–corrector method (Muppidi 2006). The scalar field is first advanced using a second-order central difference scheme. The predicted scalar field is corrected in regions of scalar overshoot using a first-order upwind scheme. This corrector step ensures that locally the passive scalar concentration is bounded (i.e. $C \in [0, 1]$). The scalar is advanced in time explicitly using a second-order Adam–Bashforth scheme in an inner loop.

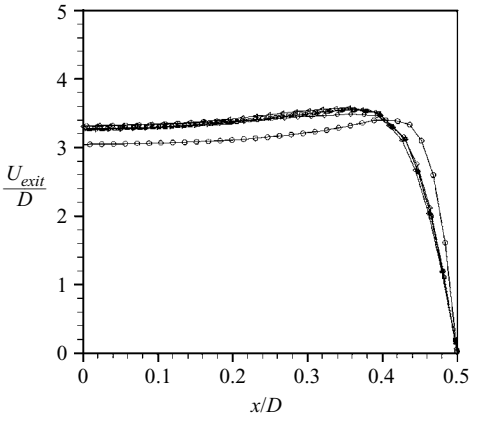

FIGURE 2. The velocity profile at the exit of the nozzle: $-\bigcirc-$, $t^* = 0.50$; $-\diamond-$, $t^* = 0.95$; $-\triangleleft-$, $t^* = 1.50$; $-\triangleright-$, $t^* = 2.50$; $-\triangle-$, $t^* = 4.00$; $-\square-$, $t^* = 5.50$;

The computational domain above the nozzle exit spans $16D \times 24D \times 16D$. The domain includes the $10D$ length of nozzle upstream of the nozzle exit. The computational mesh is unstructured and hexahedral elements are used. Figure 1(b) shows a horizontal slice of the mesh. Note the very fine elements near the nozzle exit. The boundary conditions are specified as follows. Wall boundary conditions (i.e. $u_i = 0$) are specified at the nozzle wall, outer walls ($x/D = \pm 8$ and $z/D = \pm 8$) and wall at the nozzle exit plane. The wall at the nozzle exit plane is the $y/D = 0$ plane excluding the nozzle exit surface. At the nozzle inflow plane ($y/D = -10$ plane), a top-hat velocity profile is specified:

$$v_{inflow} = \begin{cases} U_{in} & \text{if } t \leqslant \tau \\ 0 & \text{if } t > \tau. \end{cases}$$

The corresponding velocity profile at the nozzle exit is shown in figure 2 for $L/D = 6$. A zero-gradient boundary condition is used at the outflow ($y/D = 24$).

3. Results

3.1. *Comparison to experiment*

The simulation results are compared to experiment. The total circulation in the flow is compared to Gharib *et al.* (1998), which serves to validate the present simulation, as well as to give the formation number for the nozzle–wall configuration. We also compare diffusive entrainment by the vortex ring to the experiments of Dabiri & Gharib (2004).

3.1.1. *Formation number*

Figure 3(a) shows vorticity contours for two vortex rings generated by stroke ratios of 6 and 2 respectively. In the case of the higher stroke ratio, a vortex ring is generated followed by a trailing column of fluid (figure 3a). The time evolution of the total circulation, and vortex circulation are shown in figure 3(b) for $L/D = 6$. Total circulation is computed by integrating the vorticity in the plane, $z = 0$, above the nozzle exit. The vortex circulation is estimated only after it clearly pinches off from the trailing jet. The vorticity contour level that is used to determine the pinch off is set to 5 % of the maximum vorticity contour level. The pinch-off occurs in this case at

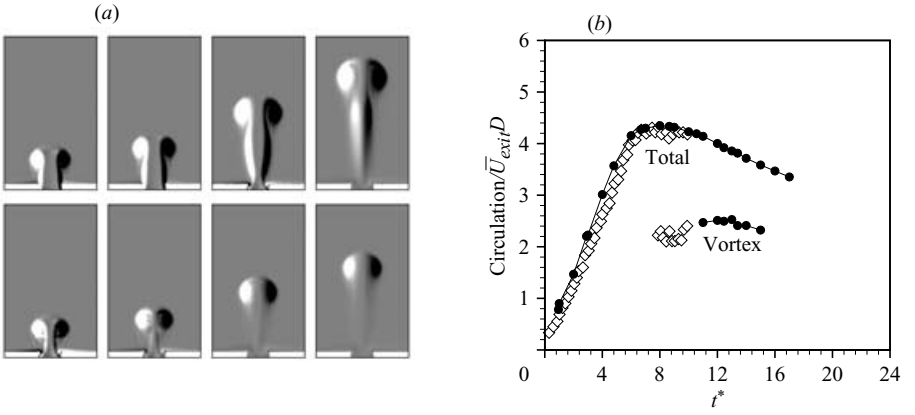

FIGURE 3. (*a*) Evolution of the vorticity field during formation and post-formation phases of the vortex ring for $L/D = 6$ (top row) and $L/D = 2$ (bottom row). The formation time instants are 3.0, 4.0, 7.0 and 10.0 (from the left). Note the vortex ring with a 'trailing column' for the higher stroke ratio. (*b*) Time evolution of the total and vortex circulation for $L/D = 6$: ◇, experiment (Gharib *et al.* 1998);—●-, simulation.

around $t^* = 11$. Thus, the leading vortex circulation is estimated from $t^* = 11$ onwards. The formation number defined by Gharib *et al.* (1998), is 'the formation time when the total circulation imparted by the discharging flow is equal to the circulation of the pinched off vortex ring'. Their study showed the existence of a limiting value for the stroke ratio (L/D), above which the vortex ring does not absorb all the vorticity of the discharged fluid. They conclude that there is a maximum value of circulation that a vortex ring can acquire as the stroke ratio increases. This maximum is reached at a piston stroke ratio of $L/D \approx 4$. If the piston stroke ratio is higher than the formation number, the excess circulation accumulates in the jet-like trailing column as shown in figure 3(*a*). For stroke ratio less than the formation number, a single vortex ring is generated, leaving behind a quiescent flow. In the simulation, the formation number is found to be approximately 3.6 from the circulation plot in figure 3(*b*). Also shown are results from Gharib *et al.* (1998) experiments. Good agreement with experiment is observed.

3.1.2. *Diffusive entrainment*

Dabiri & Gharib (2004) computed the diffusive entrainment by an isolated vortex ring after formation. The difficulty in computing entrainment is the proper definition of the unsteady boundary of the vortex ring as it propagates. This difficulty can be overcome by changing the frame of reference. Figure 4(*a*) shows the instantaneous streamline in the global frame of reference. The boundary of the vortex ring is not well defined. Figure 4(*b*) shows the instantaneous streamlines in a reference frame that moves with the vortex ring, which is done by superimposing a free-stream axial flow with magnitude equal to the measured ring axial velocity. The ring velocity was measured at the axial location of the maximum vorticity in the core of the vortex ring. The bounding streamline, 'vortex bubble', defines the visible extent of the vortex ring. The 'vortex bubble' is approximated as an ellipsoid to compute the volume, $V_B(t)$, from the measured locations of the front and rear stagnation points as well as the radial extent of the ring. This visualization and measurement of the volume of the 'vortex bubble' is suggested by Dabiri & Gharib (2004).

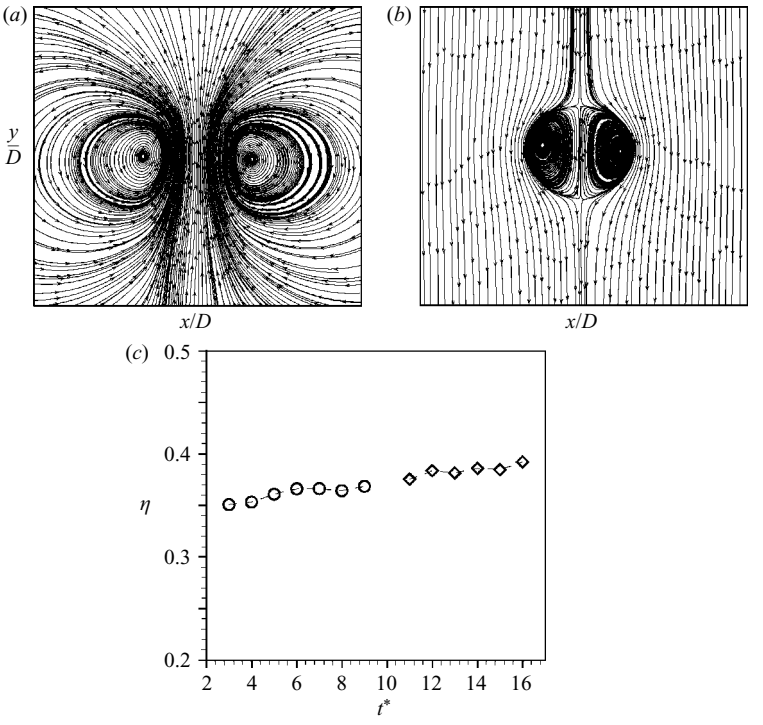

FIGURE 4. (*a*) Instantaneous streamlines. (*b*) Instantaneous streamlines in a reference frame that moves with the vortex ring. The limiting streamline shows the extent of the vortex ring or 'vortex bubble'. (*c*) The computed entrainment fraction using the 'vortex bubble' approach for two different stroke ratios: -○-, $L/D = 2$; -◇-, $L/D = 4$.

The entrainment fluid fraction $\eta(t)$ is defined by $\eta(t) = (V_B(t) - V_N(t))/V_B(t)$, where $V_B(t)$ is the volume of the vortex bubble and $V_N(t) = A \int_0^\tau U_{in}\, \mathrm{d}\tau$ is the fluid volume supplied by the nozzle. Note that the entrainment is computed using the difference between the bubble volume and the ejected volume. This definition assumes that nearly all of the ejected fluid is entrained into the ring for low stroke ratios. Figure 4(*c*) shows the entrainment fraction computed for stroke ratios $L/D = 2, 4$ and plotted against the non-dimensional time t^*. The transient volumes are computed a long time after the formation phase so that the 'vortex bubble' is completely formed. Again the objective here is to compute the diffusive fluid entrainment after the vortex ring formation. Dabiri & Gharib suggested that the entrainment fraction lies between 30 % to 40 % in these two cases. Müller & Didden (1980) estimated the entrainment fraction to be approximately 40 % in their experiment. In both our cases, the computed entrainment fractions lie between 30 % to 40 % which agree well with the experimental results.

3.2. *Scalar mixing*

The transport of passive scalar is used to study the mixing in vortex rings. The Schmidt number Sc of the scalar is 1.0.

3.2.1. *Scalar field*

Figures 5 and 6 compare instantaneous scalar contours on the symmetry plane ($z = 0$) for stroke ratios equal to 2 and 6. The scalar profiles show three distinct regions. In the ring core, boundary layer fluid from the nozzle is stretched, and mixed

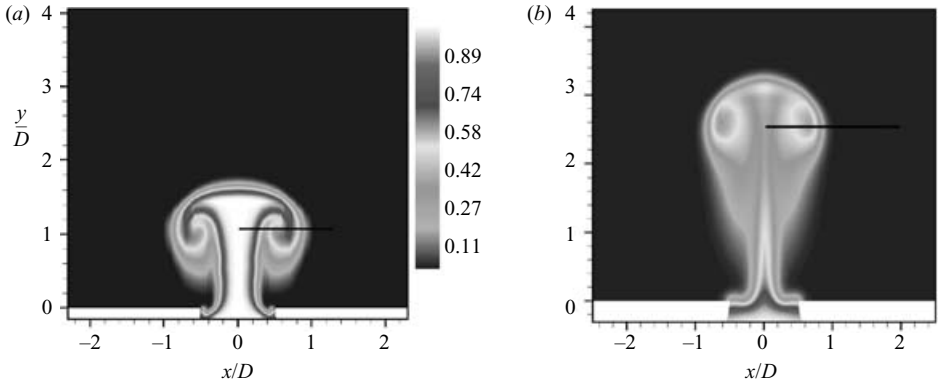

FIGURE 5. Instantaneous contours of passive scalar on the $z = 0$ plane for $L/D = 2$ at $t^* = (a)$ 3.024, (b) 6.552. Note the scalar mixing in the core of the vortex ring and downstream scalar deposition as the vortex ring propagates.

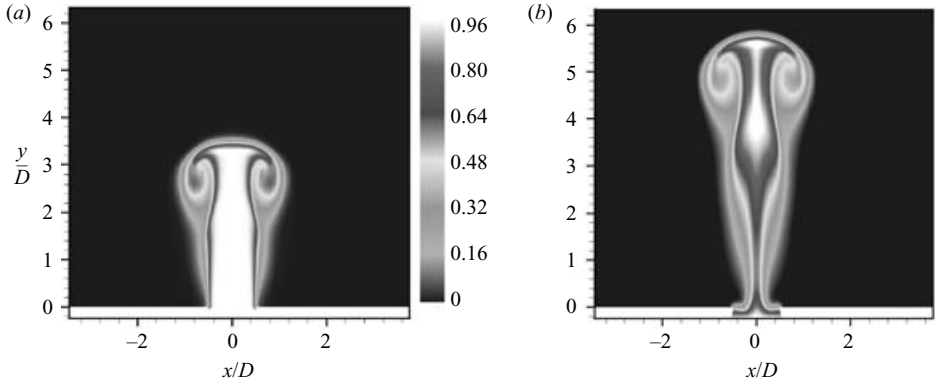

FIGURE 6. Instantaneous contours of passive scalar on the $z = 0$ plane for $L/D = 6$ at $t^* =$ (a) 6.048 and (b) 10.08. Note the trailing column behind the vortex ring.

with entrained ambient fluid. Details of the entrainment of ambient fluid are discussed in the next section. At the boundary of the ring, the scalar diffuses because of the gradient between ring fluid and the ambient fluid. This diffused scalar is deposited by the ring in its wake (low-velocity region), by a combination of its rotational velocity around the toroidal core, and its own propagation velocity. The amount of this fluid in the wake increases as the ring propagates. Similar downstream scalar deposition is observed by James & Madnia (1996). The fluid in the region surrounded by the toroidal core is mixed by diffusion because of the gradient at the interface of this region and toroidal core. The scalar in the trailing jet also diffuses into the ambient fluid.

The evolution of scalar inside the vortex ring can be quantitatively studied by examining profiles of the scalar along the line (shown in figures 5*a* and 5*b*) passing through the centre (position of maximum vorticity) of the toroidal core of the vortex ring. Figures 7(*a*) and 7(*b*) show one half of the scalar profiles (the other half is identical) for $L/D = 2$ and $L/D = 6$. The curves corresponds to different time instants after ring formation. The peak scalar concentration is equal to 1.0 across almost half the radial extent of the ring at $t^* = 2.016$ for $L/D = 2$ in figure 7(*a*). Past $x \sim 0.5D$, there is a sudden drop in the concentration. This is due to the ambient fluid entrained during

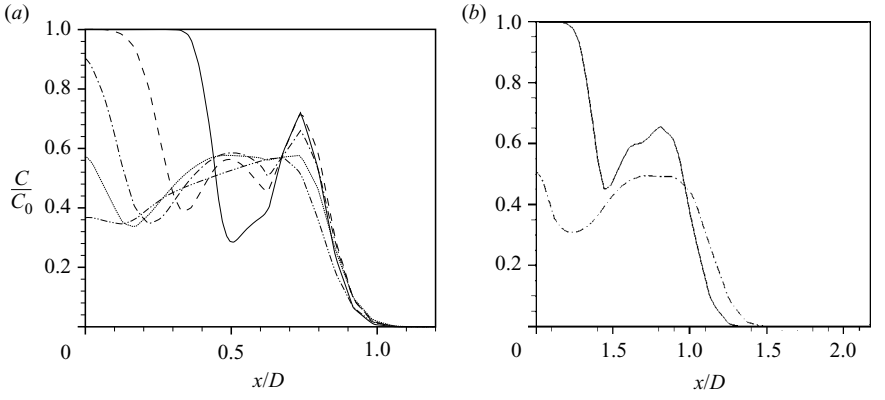

FIGURE 7. (*a*) Time evolution of the variation of scalar concentration along the line passing through the cores of the vortex ring for $L/D = 2$: ———, $t^* = 2.016$; – – – –, $t^* = 3.024$; —·—, $t^* = 4.032$; ·····, $t^* = 5.040$; —··—, $t^* = 6.552$. (*b*) Radial variation of scalar concentration along the line passing through the cores of the vortex ring for $L/D = 6$: ———, $t^* = 5.04$; —·—, $t^* = 14.1$.

the formation phase. The small region ($0.65 < x/D < 0.85$) towards the boundary of the ring is filled with stretched boundary layer fluid from the nozzle and the gradients near this region are sharp as expected. At later times, the width of the region containing peak scalar concentration near the axis of symmetry decreases rapidly. Scalar contours and profiles for $L/D = 2$ suggest that the vortex core is a region of significant mixing during the initial phases. However, at a later time after formation, the maximum scalar concentration is found near the core region of the ring. At $t^* = 6.552$, the sharp gradients inside the vortex ring have disappeared, and peak scalar concentration is observed around the core of the vortex ring. These profiles flatten at later times. Note that past $x/D = 1$, the scalar concentration is negligible even when the ring propagates. One would expect viscous diffusion to gradually increase the scalar concentration beyond $x/D = 1$. The reason for this behaviour is that the time scale of ring propagation is faster than the diffusion time scale. As a result, scalar that diffuses from the edge of the ring is deposited in the wake of the ring. Figure 5(*b*) shows that there is a considerable amount of scalar deposition on the downstream side of the ring for $L/D = 2$. Note that global conservation of the scalar was confirmed by computing the average scalar concentration $\bar{c} = (\int_V C \, \mathrm{d}V)/V$, where V denotes the volume of the domain. For all stroke ratios, $\bar{c}$ was found to be constant after the inflow stops.

The scalar field is quite different in the case of $L/D = 6$. The basic difference is that not all the scalar-carrying fluid issuing from the nozzle goes into the vortex ring. Scalar contours in figure 6 shows a trailing column of very high scalar concentration. The scalar profiles in figures 7(*a*) and 7(*b*) suggest that the qualitative behaviour of the scalar field inside the vortex ring is similar for both cases of stroke ratios. But the mixing process is much slower in the case of $L/D = 6$ than $L/D = 2$. For example, the profile at $t^* = 5.04$ for $L/D = 2$ in figure 7(*a*) is qualitatively similar to the profile at $t^* = 14.1$ for $L/D = 6$ in figure 7(*b*). The vortex ring with $L/D = 6$ takes a much longer time to attain a similar scalar profile inside the vortex ring.

3.2.2. *Entrainment during formation*

Figure 8(*a*) shows the instantaneous streamlines in the near field for $L/D = 2$ at $t^* = 1.008$, and the u-velocity profile and scalar concentration along the line AA'

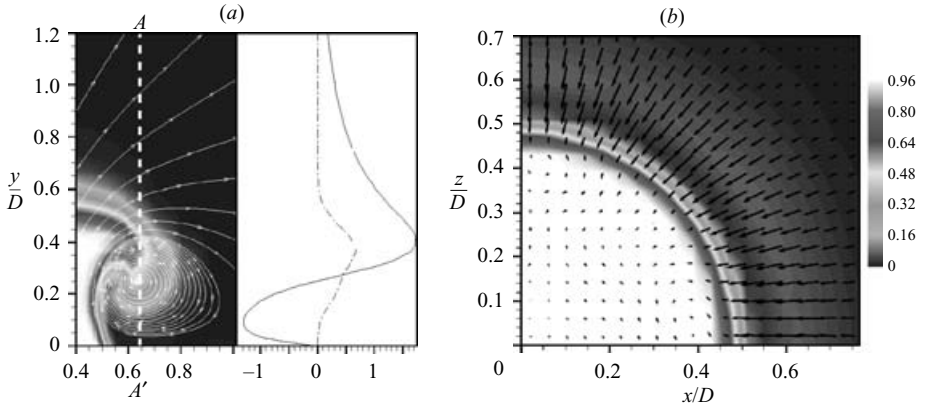

FIGURE 8. (*a*) (Left) Instantaneous streamlines on the ($z = 0$) plane along with contours of scalar for $L/D = 2$ at $t^* = 1.008$. (Right) Variation of u velocity and scalar concentration along the line AA' at $t^* = 1.008$: ———, u/D; —·—, C/C_0 scalar concentration. (*b*) A horizontal cross-section of the flow field at $y/D = 0.1$ at $t^* = 1.008$. Contours of scalar along with in-plane velocity vectors. Note the length and direction of the velocity vectors in the ambient field.

(shown as dotted white line). As the ring forms ($t^* < 2.0$ in this case), a region of very low pressure is created just outside the nozzle, at the centre of the vortex core. The resulting pressure gradient is directed towards the vortex centre, and causes ambient fluid to be entrained. This behaviour is illustrated in figure 8(*b*), which shows strong negative u-velocities near the nozzle exit, close to the wall. The scalar concentration of the fluid with negative u-velocity near the wall is close to zero, indicating ambient fluid. Figure 8(*b*) shows a horizontal cross-section at $t^* = 1.008$ at a height of $y/D = 0.1$. Velocity vectors are shown along with scalar contours. The velocity vectors show the motion of the ambient fluid toward the edge of the fluid emanating from the nozzle exit. These results show that ambient fluid is radially entrained into the vortex ring, from the near field of the nozzle, during the formation phase.

The case of large stroke ratio ($L/D = 6$) is similar until $t^* \sim 3.6$ (formation number). After this time, fluid from the nozzle cannot enter the vortex ring, and instead forms a trailing jet behind the vortex ring. The vortex ring is largest in size when the stroke ratio equals the formation number. During formation, the vortex ring entrains ambient fluid as explained earlier. However, the trailing jet does not entrain ambient fluid. Figure 9(*a*) shows the u-velocity and scalar concentration profiles along the line BB' passing through the core of the vortex ring with $L/D = 6$ at $t^* = 5.04$. Note that the u-velocity is almost zero near the trailing column up to a height of $y/D = 1$. Figure 9(*b*) shows a horizontal cross-section of the trailing jet at $y/D = 0.6$ for $L/D = 6$ at $t^* = 5.04$. The absence of appreciable radial entrainment is apparent; the trailing column is mainly surrounded by stationary fluid.

The implication is that if the objective is to maximize mixing, it is best to avoid producing the trailing column, so that entrainment can be maximized. A vortex produced with stroke ratio equal to the formation number entrains the most ambient fluid for a given amount of fluid in the nozzle. The volume of fluid required for stroke ratio equal to 6 is three times the volume required to create a single vortex ring of stroke ratio 2. The above results suggest that it would be better to create three successive vortex rings with $L/D = 2$, or two successive vortex rings of stroke

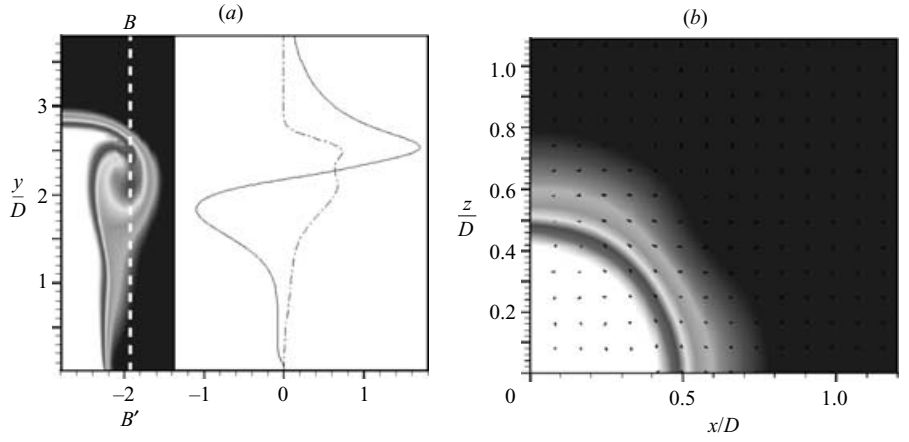

FIGURE 9. (*a*) $L/D = 6$ at $t^* = 5.04$, variation of u velocity and scalar concentration along the line BB' (dotted white line): ———, u/D; —·—, C/C_0 scalar concentration. (*b*) A horizontal cross–section of the trailing jet at $y/D = 0.6$ at $t^* = 5.04$. Contours of scalar along with in-plane velocity vectors. Note that the in-plane velocity vectors are of zero magnitude. The same scalar contour levels are used here as in figure 8.

ratios equal to 3.6 (formation number) and 2.4, instead of a single vortex ring with $L/D = 6$. This conclusion, of course ignores any interaction between the rings.

3.2.3. *Rate of mixing*

Figure 10(*a*) shows the time variation of the total volume of scalar-containing fluid (V_{sc}) for stroke ratios equal to 2 and 6. V_{sc} is computed as the sum of all volume elements which have scalar concentrations above a threshold value (set to 0.01) in the domain above the nozzle exit plane ($y/D > 0$). The threshold value of scalar concentration allows the difference between the scalar-containing fluid and unmixed ambient fluid to be represented. V_{sc} can be considered as a measure of the spread of the scalar in the flow field. Figure 10(*a*) shows that V_{sc} increases nearly linearly (at a rate of 1.7) until $t^* \sim 2$. In general, V_{sc} increases due to diffusion of scalar from the boundaries of the ring, and mixing of entrained ambient fluid inside the vortex ring. During the very short time ($t^* \leqslant 2$) of ring formation, entrainment of ambient fluid dominates, as discussed earlier. The linear rate of increase in V_{sc} is therefore mostly a result of mixing of ambient fluid with nozzle fluid, in the toroidal core of the ring.

After the inflow stops ($t^* > L/D$), V_{sc} further increases, as shown in figure 10(*a*). This increase is also nearly linear, and its slope, $\mathrm{d}V_{sc}/\mathrm{d}t^*$ yields the rate of volume mixing when the vortex ring propagates. Figure 10(*b*) plots $\mathrm{d}V_{sc}/\mathrm{d}t^*$ after formation ($t^* > L/D$) for different stroke ratios. Note that the rate increases linearly with stroke ratio until the stroke ratio equals the formation number. For stroke ratios greater than the formation number, the rate falls below the linear curve. The deviation increases with increasing stroke ratio, and may be explained as follows.

Recall that stroke ratios smaller than the formation number yield a vortex ring without a trailing column. The size of the vortex ring increases with increasing stroke ratio, until the formation number is reached, since nearly all of the nozzle fluid goes into the vortex ring. The largest possible vortex ring is therefore produced at the formation number. This increase in ring size results in an increased rate of mixing. As the stroke ratio increases beyond the formation number, the flow field consists of the leading vortex ring, and a trailing column. Increasing the stroke ratio does not

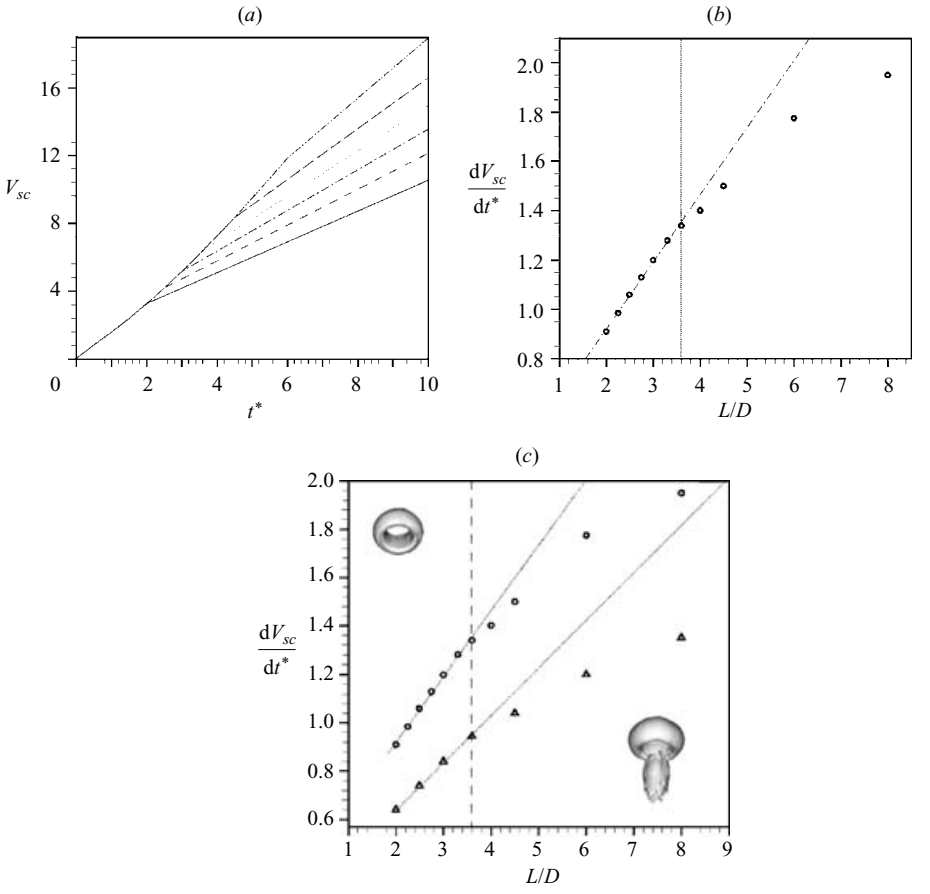

FIGURE 10. (*a*) Plot of volume of scalar-carrying fluid with time for different stroke ratios: ———, $L/D = 2.0$; – – – –, $L/D = 2.5$; — · —, $L/D = 3.0$; · · · · · · · · , $L/D = 3.6$; – – –, $L/D = 4.5$; — · · —, $L/D = 6$. (*b*) The rate of scalar volume after formation is plotted against the stroke ratio. The dotted line separates the two regime of flow: stroke ratio less than formation number and higher than formation number. (*c*) The rate of scalar volume is plotted against the stroke ratio for two different Schmidt numbers: ○, $Sc = 1$; △, $Sc = 10$. The corresponding flow structures (iso-surface of vorticity) are also shown for the two regimes.

change the leading vortex ring; it only increases the length of the trailing column. The overall entrainment may be thought to be a combination of entrainment by the leading vortex ring, and entrainment by the trailing column. The relative contribution of the leading vortex ring to the overall entrainment therefore decreases as the stroke ratio increases. Recall that the trailing column does not entrain fluid as effectively as the vortex ring. This results in an overall decrease of entrainment as the stroke ratio increases beyond the formation number.

The qualitative dependence of the rate of change of scalar-carrying fluid on stroke ratio is found to be independent of Schmidt number Sc. Figure 10(*c*) shows results for Schmidt numbers of 1 and 10. Even for $Sc = 10$, the rate increases linearly with stroke ratio until formation number, and deviates away from the linear curve for stroke ratios higher than formation number. The scalar diffuses less at higher Schmidt number, which leads to a lower rate at the same stroke ratio. Since entrainment does

not depend on Schmidt number, the qualitative behaviour of the curves shown in figure 10(*c*) does not change with Schmidt number.

4. Summary

Direct numerical simulation of passive scalar mixing in vortex rings has been performed, and the effect of stroke ratio on entrainment and mixing is examined. Computed results for circulation and formation number agree well with experimental values. Instantaneous scalar profiles inside the vortex rings are used to compare the mixing in vortex rings whose stroke ratio is smaller than the formation number to rings whose stroke ratio is greater. The results show the spiral roll-up of nozzle fluid, and its mixing with entrained ambient fluid in the toroidal core of the ring. As the ring forms, it rapidly entrains ambient fluid from the near field of the nozzle exit. For stroke ratios greater than the formation number, this entrainment is completely absent in the trailing column. The rate of change of scalar-carrying fluid after ring formation was examined, and seen to vary linearly with stroke ratio until the formation number is reached. As the stroke ratio increases beyond the formation number, the rate increasingly deviates away from the linear curve. This suggests that the generation of the trailing column is best avoided, if the objective is to entrain and mix as much as ambient fluid as possible. The present results suggest that the frequency and duty cycle of pulsed jets should be such that the effective stroke ratio is near the formation number or at least not larger than formation number. Note however, that our conclusions strictly apply only to a single vortex ring in stationary fluid; they do not account for the possible effects of interaction among successive rings, and interaction with the crossflow.

This work was supported by the National Science Foundation under grant CTS–0133837. Computer time was provided by the National Center for Supercomputing Applications (NCSA), Minnesota Supercomputing Institute (MSI) and the San Diego Supercomputer Center (SDSC). We thank Dr Suman Muppidi for helpful discussions.

REFERENCES

Dabiri, J. O. & Gharib, M. 2004 Fluid entrainment by isolated vortex rings. *J. Fluid Mech.* **511**, 311–331.

Didden, N. 1979 On the formation of vortex rings: Rolling–up and production of circulation. *Z. Angew. Mech. Phys.* **30**, 101–116.

Eroglu, A. & Briedenthal, R. E. 2001 Structure, penetration and mixing of pulsed jets in crossflow. *AIAA J.* **39**, 417–423.

Gharib, M., Rambod, E. & Shariff, K. 1998 A universal time scale for vortex ring formation. *J. Fluid Mech.* **360**, 121–140.

Glezer, A. 1988 The formation of vortex rings. *Phys. Fluids* **31**, 3532–3542.

James, S. & Madnia, K. 1996 Direct Numerical Simulation of a laminar vortex ring. *Phys. Fluids* **8**, 2400–2414.

Johari, H., Pacheco-Tougas, M. & Hermanson, J. C. 1999 Penetration and mixing of fully modulated turbulent jets in crossflow. *AIAA J.* **37(7)**, 842-850.

Liepmann, D. & Gharib, M. 1992 The role of streamwise vorticity in the near-field entrainment of round jets. *J. Fluid Mech.* **245** 643-668.

Mahesh, K., Constantinescu, G. & Moin, P. 2004 A numerical method for large–eddy simulation in complex geometries. *J. Comput. Phys.* **197**, 215–240.

Maxworthy, T. 1972 The structure and stability of vortex rings. *J. Fluid Mech.* **51**, 15–32.

Maxworthy, T. 1977 Some experimental studies of vortex rings. *J. Fluid Mech.* **81**, 465–495.

M'Closkey, R. T., King, J. M., Cortelezzi, L. & Karagozian, A. R. 2002 The actively controlled jet in crossflow. *J. Fluid Mech.* **452** 325–335.

Muppidi, S. 2006 Direct numerical simulations and modeling of jets in crossflow. PhD Thesis, University of Minnesota.

Müller, E. A. & Didden, N. 1980 Zur erzeugung der zirkulation bei der bildung eines ringwirbels an einer dusenmundung. *Stroj. Casop.* **31**, 363–372.

Rosenfeld, M., Rambod, E. & Gharib, M. 1998 Circulation and formation number of laminar vortex rings. *J. Fluid Mech.* **376**, 297–318.

Shariff, K. & Leonard, A. 1992 Vortex rings. *Annu. Rev. Fluid Mech.* **24**, 235–279.

Vermeulen, P. J., Rainville, P. & Ramesh, V. 1992 Measurements of the entrainment coefficient of acoustically pulsed axisymmetric free air jets. *J. Engng Gas Turbines Power* **114**, 409–415.

Vermeulen, P. J., Ramesh, V. & Yu, W. K. 1986 Measurements of entrainment by acoustically pulsed axisymmetric air jets. *J. Engng for Gas Turbines Power* **108**, 479–484.